Radar Observations of Humidity Variability in and above the Marine Atmospheric Boundary Layer

ALLEN B. WHITE

Cooperative Institute for Research in Environmental Sciences, University of Colorado at Boulder, Boulder, Colorado

C. W. FAIRALL

Wave Propagation Laboratory, National Oceanic and Atmospheric Administration, Boulder, Colorado

DENNIS W. THOMSON

Department of Meteorology, The Pennsylvania State University, University Park, Pennsylvania

(Manuscript received 10 September 1990, in final form 7 March 1991)

ABSTRACT

Humidity variability at the top of the marine atmospheric boundary layer and in the overlying free troposphere was examined using data collected during the marine stratocumulus phase of the First Regional Experiment (FIRE) of the International Satellite Cloud Climatology Program. A time series of the humidity structure-function parameter C_q^2 derived from Doppler wind profiler reflectivity data is compared to a concurrent time series of specific humidity q. Both q and its vertical gradient were calculated from rawinsonde data obtained from sondes launched within 500 m of the profiler. Time–height correlation analysis between $\log(C_q^2)$ and $\log(\partial q/\partial z)^2$ shows that the two time series are highly correlated at and just above the inversion base, with r approximately equal to 0.7. The correlation is slightly lower in the free troposphere where r is about 0.5 (a value of r greater than 0.2 is significant at the 95% confidence level). There is also correlation between $\log(C_q^2)$ and $\log(q)$, which is maximized at an offset in height between the two instruments.

Closer analysis of a short-lived clearing event shows locally reduced values of C_q^2 in a region of enhanced $\partial q/\partial z$. This apparent paradox can be explained by noting the absence of enhanced entrainment associated with cloud-top radiative cooling. The combined wind profiler–rawinsonde datasets were also used to estimate the entrainment velocity w_e for clear and cloudy conditions. An average value of w_e equal to 0.38 cm s^{-1} was obtained for cloudy conditions; for the clear case a value of 0.13 cm s^{-1} was obtained.

1. Introduction

The intensive field operations (IFO) of the marine stratocumulus phase of the First Regional Experiment (FIRE) took place during June–July 1987 off the coast of southern California. A comprehensive dataset was obtained from a variety of platforms. These included surface-based remote sensors for detailing the structure and properties of the marine atmospheric boundary layer (MABL) and stratocumulus clouds. Operations during the FIRE IFO are summarized by Albrecht et al. (1988) and Kloesel et al. (1988). Most of the ground-based systems were sited on San Nicolas Island (SNI), located approximately 100 km west-southwest of Los Angeles, California.

Corresponding author address: Mr. Allen B. White, NOAA/Environmental Research Laboratories, Mail Code R/E/WP7, 325 Broadway, Boulder, CO 80303.

During the FIRE IFO, scientists from Pennsylvania State University operated a 404-MHz UHF Doppler wind profiler at SNI. Profiles of three wind components and backscatter intensity were recorded at 2-min intervals. During the same period, scientists from Colorado State University (CSU) operated a cross-chain loran atmospheric sounding system (CLASS) within 0.5 km of the wind profiler site. A total of 69 soundings were taken at launch frequencies ranging from 2 to 10 per day. Raw data from the PTU (pressure, temperature, relative humidity) sensor were used to calculate meteorological variables (q, θ_v) in the standard way. Vertical profiles of the CLASS data and information about the system are presented in Schubert et al. (1987a).

This paper reports variations in the humidity structure that were identified in the analysis of UHF Doppler wind profiler reflectivity and conventional rawinsonde data logged at SNI. For this discussion, a 5-day period from 1200 UTC 10 July to 1200 UTC 15 July was

used. This period was chosen primarily because of the increased frequency of rawinsonde launches. Additionally, the marine inversion was unusually high and fell above the minimum detectable range (MDR) of the radar (MDR $\approx$ 600 m).

This paper also evaluates the use of a clear-air Doppler radar to determine details of humidity structure. Vertical profiles of radar reflectivity are used to quantify the turbulent humidity structure through conversion of the radar refractive index structure parameter C_n^2 to the humidity structure parameter C_q^2. These turbulence data were time-averaged and then correlated with the mean humidity structure determined from rawinsonde profiles.

Finally, values of radar C_q^2 near the inversion were combined with the appropriate variables derived from rawinsonde data to produce a time series of the entrainment velocity w_e. The average radar-derived entrainment rate for the entire analysis period is compared to the value of w_e calculated from an inversion height budget model.

2. The UHF Doppler wind profiler

The UHF wind profiler used at FIRE was built at Pennsylvania State University. The radio frequency components were purchased from Tycho Technology, Inc. The system design, computer interface hardware, and system software were modeled on the technology developed at the NOAA Wave Propagation Laboratory (Strauch et al. 1984). The radar's antenna system consists of two phased-array, coaxial-collinear (CoCo) antennas. Each antenna contains a set of 16 parallel elements, 6.7 m long. The two antennas are normally oriented orthogonally to one another. This configuration combined with a prescribed, switchable phasing in the antenna elements produces three beams (one zenith, two off-zenith). The radar reflectivities used here were recorded by the off-zenith beam that was judged to have the best signal-to-noise ratio (SNR) characteristics.

Operating parameters for the UHF wind profiler are summarized in Table 1. The radar frequency is 404.37 MHz (wavelength = 0.742 m in air). For the SNI experiment, the radar was operated using only the shortest pulse length (1 μs), which corresponds to a range resolution of $\Delta R \approx 150$ m. This selection was made to gather as much data as possible from the MABL and the altitudes just above the inversion.

TABLE 1. FIRE UHF wind profiler parameters.

Symbol	Parameter	Value
A_e	effective antenna area (one section) assumed equal to geometrical area	47.0 m^2
E	efficiency of the radar antenna and transmission line	0.10
f	radar frequency	404.37 MHz
λ	wavelength	0.742 m
	two-way beamwidth	$\approx$15°
P_t	peak pulse power	8.0 kW
τ	pulse width	1.0 μs
ΔR	range resolution	149.9 m
F_r	pulse-repetition frequency	10 kHz
N_c	number of coherent integrations (time-domain averaging)	288
B	bandwidth of integrating filter ($B = F_r/N_c$)	34.7 Hz
N_f	number of fast Fourier transform points	64
N_s	number of spectra averaged	8
Δx	antenna-element spacing	0.3125 m
χ	off-vertical beam axis angle	14.5°
T_{rx}	receiver-noise temperature	100 K
T_c	cosmic-noise temperature	10–100 K

3. C_n^2 and the Doppler radar reflectivity equation

The returned backscatter power received by the radar is directly proportional to the refractive-index structure parameter C_n^2 (VanZandt et al. 1978). This quantity can be related to other quantities, such as C_q^2, that relate the meteorological state variables to the turbulent structure of the atmosphere. If it is assumed that refractive-index irregularities are in equilibrium with steady-state turbulence and that the transmitted wavelength λ lies within the inertial subrange of turbulence, then C_n^2 can be computed from the radar reflectivity or scattering cross section per unit volume η measured by the radar (Ottersten 1969a):

$$\eta = 0.38 C_n^2 \lambda^{-1/3}. \tag{3.1}$$

Variations in the radio refractive index can result from fluctuations in temperature, humidity, and pressure. Pressure fluctuations can generally be ignored (Burk 1980). Following Ottersten (1969b), the refractive-index gradient M may be written as

$$M = 6 \times 10^{-4} P/T^2 [q' - 0.13(1 + 15.5q/T)T'], \tag{3.2}$$

where P is the pressure in millibars, T is the temperature in kelvins, q is the specific humidity in grams per kilogram, and the prime (′) denotes a vertical derivative. In terms of the scalar structure-function parameters, this dependence can be expressed as (Wesely 1976; Burk 1980)

$$C_n^2 = (6 \times 10^{-4} P/T^2)^2 C_q^2 \alpha_r^2, \tag{3.3}$$

where

$$\alpha_r^2 = 1 - 2a r_{Tq} C_T/C_q + a^2 C_T^2/C_q^2. \tag{3.4}$$

Here C_T^2 is the temperature structure-function parameter, r_{Tq} is the temperature–moisture correlation coefficient, and

$$a = 0.13(1 + 15.5\bar{q}/\bar{T}). \tag{3.5}$$

The quantity $(\alpha_r^2 - 1)$ gives the deviations from pure moisture dominated C_n^2.

Wesely (1976) developed the functions describing the relative contributions of C_q^2 and C_T^2 to C_n^2 for electromagnetic and acoustic radiation. Burk (1980) later evaluated these expressions using a second-moment turbulence closure model for one overland and two MABL simulations. The MABL cases predicted that radar C_n^2 would be dominated throughout the MABL by C_q^2 (i.e., $\alpha_r^2 \approx 1$). Above the boundary layer, C_n^2 is typically dominated by C_q^2 to altitudes of a few kilometers (VanZandt et al. 1978). In the upper troposphere and stratosphere, C_n^2 is dominated by C_T^2.

For the analysis presented later in this paper, an approximation will be made that states C_n^2 is directly proportional to C_q^2 using a median profile of α_r^2 computed for the entire experiment. The conditions being dealt with are the lower 2.1 km of the atmosphere with a marine boundary layer depth of 0.4–1.2 km. The boundary layer is typically slightly unstable and is topped with stratocumulus clouds most of the time. In the absence of temperature contributions, the temperature error factor, $(\alpha_r^2 - 1)$, is zero. Because of the differing dynamics, we must examine the magnitude of α_r^2 separately for the boundary layer and the free troposphere. This issue will be discussed further in section 6.

The approximate relationship of C_n^2 to C_q^2 is found by rearranging (3.3);

$$C_q^2 = (1.66 \times 10^3 T^2/P)^2 \alpha_r^{-2} C_n^2, \quad (3.6)$$

where $T = 288$ K, $P \approx P_0 e^{(-z/H)}$ is the pressure in millibars, z is the altitude in kilometers, $P_0 = 1000$ mb, and $H = 8$ km. Substituting (3.1) into (3.6) gives

$$C_q^2 = (1.66 \times 10^3 T^2/P)^2 \alpha_r^{-2} (\eta/0.38)\lambda^{1/3}. \quad (3.7)$$

This equation enables one to estimate the atmospheric turbulent humidity structure in the lower troposphere from radar reflectivity. However, η must still be related to a quantity directly measured by the radar.

The scattered signals received by the radar are converted into Doppler spectra, from which the SNR is estimated. Because of the complex nature of the Doppler signal processing, an unconventional radar equation is used to relate η to radar SNR. The Doppler radar reflectivity equation given by VanZandt et al. (1978) is used:

$$\eta = 9\pi c k_0 B(ET_c + T_{rx})(R^2/\Delta R^2)(\mathrm{SNR}) \times [2E^2 P_t F_r A_e \cos(\chi)]^{-1}, \quad (3.8)$$

where $c = 2.998 \times 10^8$ m s^{-1} is the speed of light in a vacuum, $k_0 = 1.3803 \times 10^{-23}$ J mol^{-1} K^{-1} is Boltzmann's constant, and R is the range. All other parameters in (3.8) are defined in Table 1.

In (3.8), noise contributions from internal- (electronic) and external- (cosmic) noise sources are expressed as noise temperatures. At $\lambda = 0.742$ m, the cosmic-noise temperature varies from about 10 K at the galactic pole to about 100 K at the galactic center (Kraus 1966). However, since ET_c is less than T_{rx}, cosmic-noise interference in the SNI data can be neglected. Combining (3.7) with (3.8) and substituting values from Table 1 gives the specific form of the radar C_q^2 equation used here:

$$C_q^2 = 1.63 \times 10^{-15}(T^2/P)^2 \alpha_r^{-2} R^2 10^{\mathrm{SNR}/10}, \quad (3.9)$$

where SNR is now in decibels (dB) as it was recorded on magnetic tape during FIRE.

4. Radar calibration

The accuracy of turbulence variables calculated from radar reflectivity data depends partly on the accuracy of the various system parameters listed in Table 1. The most important and most uncertain of these parameters is the system efficiency E, which appears in (3.8) as the squared term in the denominator. This term accounts for absorptive and radiative losses in the transmission line and antenna, as well as the gain function associated with the directivity of the antenna (VanZandt et al. 1978). An absolute calibration would therefore require direct measurement of the antenna gain function and the other losses.

Another way of calibrating the radar is to compare radar-derived values of C_n^2 to measurements made with other calibrated instruments. Two attempts were made at estimating the UHF Doppler radar system efficiency by this method. Both of these calibrations were performed after the FIRE IFO. In each case, the radar was disassembled for transport and then reassembled at the site where the calibration took place. In the first experiment, SNR data collected by the UHF radar at Pennsylvania State University during August 1988 were compared with SNR data collected by a VHF Doppler radar located about 15 km away. The VHF radar had been previously calibrated against upper tropospheric and stratospheric values of C_T^2 as determined by microthermal sensors on free balloons and research aircraft (Beecher 1988). The value of 0.35 obtained for the VHF total efficiency factor from this study was somewhat larger than the value of 0.18 determined for nearly identical NOAA systems (VanZandt et al. 1978).

Assuming that UHF and VHF radars provide the same estimate of C_n^2 at a particular height, (3.1) and (3.8) can be used to derive an expression for the UHF-system efficiency in terms of the known VHF-system efficiency, the various operating parameters, and the SNR difference logged by the two radars:

$$E_u^2 = E_v^2 (P_{tv}/P_{tu})(A_{ev}/A_{eu})(N_{cv}/N_{cu}) \times (\lambda_u/\lambda_v)^{1/3}(\tau_v/\tau_u)^2 [T_{rxu}/(E_v T_{cv} + T_{rxv})] \times 10^{[(\mathrm{SNR}_u - \mathrm{SNR}_v)/10]}, \quad (4.1)$$

where u and v refer to the UHF and VHF radars, re-

spectively. With $E_v = 0.35$, $(\mathrm{SNR}_u - \mathrm{SNR}_v) = -24.0$ dB, and the other appropriate values inserted in (4.1), the UHF-radar-system efficiency is determined; $E_u = 0.15$.

A potential problem with this method is that the samples are derived from spatially separated volumes of air that might have different refractive index structures. Our two radar sites are separated by approximately 15 km in a region that includes complex topographical features. Thus, it may not be appropriate to use SNR measurements recorded at the same time and altitude. Figure 1, which shows correlation-coefficient curves for the time series of SNR and horizontal velocity components compiled by the UHF and VHF radars, indicates that this concern is justified. The UHF SNR measurements appear to be best correlated with VHF measurements taken 300 m lower in altitude. Note that this height difference is greater than one would expect to be associated with any terrain-related meteorological phenomena; maxima mountain–valley topographical differences in the surrounding area are less than 300 m. The offset may be due to error in the heights of the VHF radar range gates. Because of this uncertainty, an additional calibration was performed.

For the second calibration (February–March 1989), the same radar used at SNI was located at Otis Air Force Base in southeastern Massachusetts. The radar had been operating in this location for several months as part of an experiment on marine cyclogenesis. In situ profiles of C_q^2 were obtained by flying an instrumented aircraft over the radar site. Using a Lyman-α hygrometric sensor, aircraft C_q^2 values were determined by the spectral method. The aircraft and instruments used for this calibration are described by Fairall and Markson (1984). Four flights were made, each usually including ascending and descending flight legs. The aircraft profiles were then compared to radar-deduced C_q^2 profiles. This calibration method has the advantage over the previous method of sampling in that almost the same volume is sampled with both instruments. However, since vertical profiles from the aircraft measurements have much coarser temporal resolution than the radar profiles, hourly averages of the radar data were used.

The median difference in structure parameter estimates for the two datasets were used to determine the UHF system efficiency. Results of this analysis are summarized in Table 2. An example profile of aircraft and radar C_q^2, with $E_u = 0.07$, is given in Fig. 2. One disadvantage of this method is that it neglects differences in the type of averaging done by instantaneously sampling a given volume and averaging point-sampled

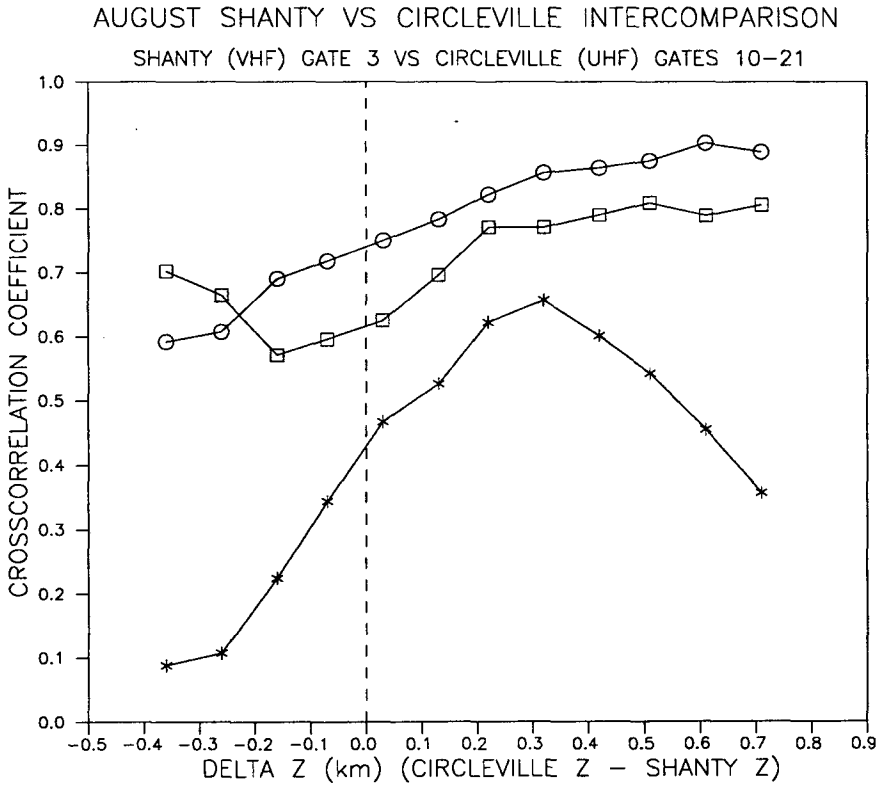

FIG. 1. Correlation as a function of vertical spacing for SNR (asterisks) and horizontal velocity measurements, U (circles) and V (squares), determined from UHF and VHF radar data.

TABLE 2. Results of the aircraft–UHF radar system efficiency calibration

Vertical range = 0.7–1.6 km
Number of data points = 36
Median E_u = 0.074
Mean E_u = 0.17
Variance = 0.089

measurements along an aircraft flight line. Obviously this comparison also relies on accurate calibration of the Lyman-α hygrometer. The calibration used here (Fairall et al. 1990a) was not applicable for the very dry conditions found above the boundary layer (hence, the large apparent disagreement between aircraft and radar values near z = 1.5 km evident in Fig. 2). Lastly, the temperature contribution to radar C_n^2 expressed in (3.3) and (3.4) is uncertain. Analysis of temperature spectra produced from time series recorded during the aircraft flights indicated operational problems with the temperature sensors. As a result, only a small fraction of the aircraft C_T^2 data recorded in the range of the radar could be used. However, even if more C_T^2 was available, the uncertainty in the sign and magnitude of r_{Tq} for the conditions encountered during the aircraft flights prevents proper evaluation of α_r^2. For these reasons, the aircraft calibration is estimated to be uncertain by about a factor of 2 in α_r^2.

Considering all the potential problems associated with performing the calibrations of the type described above, the resulting system efficiencies can be considered to agree reasonably well. For the subsequent calculations discussed here, E_u = 0.10 was chosen, a value that reflects our slightly greater confidence in the in situ aircraft calibrations. However, because of the combined uncertainties in the two calibrations, this factor is considered to be uncertain by about 40%. Since E_u enters the C_n^2 computation as the square, determinations of C_n^2 are estimated to have an absolute uncertainty of less than a factor of 2.

5. Structure function–gradient relationships and the entrainment rate

In regions of active turbulence in the stably stratified free troposphere, C_x^2 is related to the square of the vertical gradient of x by (Fairall et al. 1988)

$$C_x^2 = 1.6\gamma(C_u^2/N_b^2)(\partial x/\partial z)^2, \qquad (5.1)$$

where x can be q, T, or n; C_u^2, a measure of the local turbulence, is the velocity structure function parameter; N_b is the Brunt–Väisälä frequency; and γ = Ri/(Pr − Ri), where Ri is the Richardson number and Pr is the turbulent Prandtl number. In regions of active turbulence, Pr $\approx$ 1 and Ri $\approx$ 0.25, such that $\gamma \approx 0.3$. Within the boundary layer, the relationship between C_x^2 and $\partial x/\partial z$ is well established near the surface (see Wyngaard et al. 1971). In the mixed layer, local scalar gradients are very small and there is little relation to C_x^2 (Fairall 1987).

One of the key parameters used to evaluate the transition occurring in an inversion near cloud top is the entrainment velocity w_e, which is a measure of the growth rate of the turbulent MABL into the largely nonturbulent air above the inversion. Unfortunately, w_e is exceedingly difficult to obtain experimentally (Davidson et al. 1984). For example, in situ measurements obtained from aircraft or balloon measurements yield horizontally averaged profiles, which tend to smear out the turbulent structure. On the other hand, radar has the important advantage of providing continuous vertical profiles of deduced turbulence statistical quantities, which can be approximately related to the entrainment rate by a generalized form (Fairall 1984) of the Wyngaard–LeMone interfacial model (Wyngaard and LeMone 1980):

$$w_e = 6\Delta\theta_v \epsilon^{1/3} C_q^2 [11.2(\Delta q)^2 \Gamma]^{-1}, \qquad (5.2)$$

where θ_v is the virtual potential temperature; Γ is the lapse rate of θ_v above the inversion; Δ denotes the change in a variable across the inversion layer; ϵ is the rate of dissipation of turbulent kinetic energy in the inversion; and w_e is evaluated at the middle of the in-

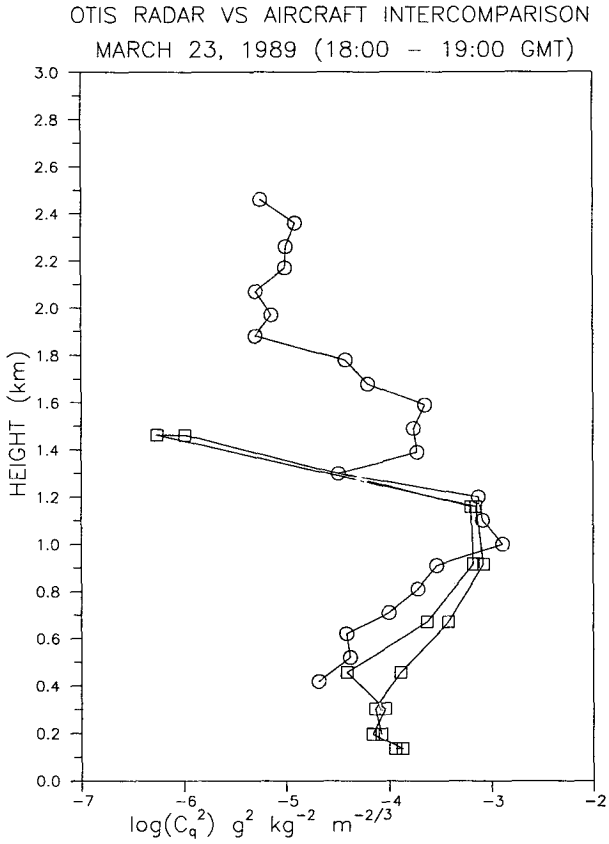

FIG. 2. Vertical profiles of $\log(C_q^2)$ calculated from radar reflectivity (circles) and in situ aircraft measurements (squares).

version interfacial layer. Although coincident measurements of ϵ may not be available during operation of the radar, a method has been demonstrated (Hocking 1983; Gossard and Sengupta 1988) that uses the spectral width of radar echoes to estimate ϵ. Thus (5.1) and (5.2) are model equations that can be used to relate radar backscatter power and spectral width to the important meteorological variables.

6. Interpretation of radar return

a. Temperature contributions to C_n^2

In the lower part of the planetary boundary layer, the structure-function profiles tend to be determined by surface-layer similarity relationships based on the surface fluxes (Fairall 1987). Burk (1980) showed that for $|r_{Tq}| \approx 1$, then $(\alpha_r - 1) = 0.46\beta$ where β is the Bowen ratio. Typical values of β over the ocean are on the order of 0.2–0.3; a value of 0.3 yields $\alpha_r^2 = 0.74$. Thus, the actual value of C_n^2 is on the order of 25% less than the pure moisture value for this case. In the upper parts of the boundary layer, entrainment and clouds play an important role in determining α_r^2. Clouds change the situation in the boundary layer in three ways: 1) condensation processes create an additional thermodynamic coupling between temperature and moisture, 2) cloud-top longwave cooling greatly increases the rate of entrainment of warm, dry air from the free troposphere, and 3) cloud and drizzle liquid water droplets provide an additional scattering mechanism for the radar.

In the absence of clouds, the top-down/bottom-up diffusion similarity model (Fairall 1987) can be used to examine the temperature contributions to C_n^2 throughout the boundary layer (marine or over land). Fairall (1991) showed that if the magnitude of the inversion Bowen ratio, defined as

$$\beta_i = c_p \Delta\theta (L_e \Delta q)^{-1}, \qquad (6.1)$$

is less than about 0.5, then the errors associated with assuming purely moisture-dominated C_n^2 will remain less than 25%. This agrees with a series of 10 aircraft profiles of C_T^2 and C_q^2 made by Fairall (1982) off California and in the Bahamas [a summary of these measurements appeared in Fairall (1984)] and also agrees with Burk's (1981) evaluation of α_r^2 in the inversion region. Because the model is not directly applicable to the cloud-topped boundary layer, details of this study will not be presented. Yet based on simple physical reasoning it is expected that the result is valid for the entrainment-induced effects associated with the clouds. This is also born out by the second-order closure model study of Burk (1980), where moisture dominated radar C_n^2 for the two MABL cases examined, even in the presence of clouds. However, in some of the SNI/FIRE cases, the inversion Bowen ratio is on the order of -0.8. Under those conditions and with sufficiently strong entrainment, C_n^2 might be as much as a factor of 1.5 larger than its pure C_q^2 associated part in the upper portion of the boundary layer.

For the free troposphere, (5.1) and the radiosonde profiles can be used to examine α_r^2. Using (5.1), we modify the α_r^2 relation

$$\alpha_r^2 = [1 - a(\partial\bar{\theta}/\partial z)(\partial\bar{q}/\partial z)^{-1}]^2, \qquad (6.2)$$

where it is assumed that $r_{Tq} = 1$ if the temperature and moisture gradients are of the same sign and $r_{Tq} = -1$ if they are of opposite sign. Note that inertial subrange correlation coefficients have not been measured in the free atmosphere, so our assumption will tend to overestimate the temperature effects if the magnitude of r_{Tq} is less than one. Figure 3 shows the mean profiles of q and θ and the resultant median α_r^2 profile computed for the analyzed period. Recall that this computation of α_r^2 is only valid above the inversion. The θ–q profiles indicate a well-mixed MABL, capped by an inversion, a free tropospheric transition layer between 1.0 and 2.2 km, and finally a more weakly stratified and drier, subsidence-dominated free troposphere above 2.2 km. It will be seen later that most of the moisture variability observed in this period occurred in the inversion and transition layers. Individual profiles generally exhibit a very sharp jump from the MABL to the transition layer. Since the inversion height varies with time, the averaging process tends to smear out the discontinuity, so the inversion occupies the region between about 0.6 and 1 km.

The free tropospheric (i.e., nonboundary layer) part of the radar sample volume is contained entirely within this transition layer. The transition layer has a mean potential temperature gradient of approximately 5 K km^{-1}. The humidity profile has a roughly exponential decrease with height. In the transition layer, the gradient is characterized by

$$(1/\bar{q})(\partial\bar{q}/\partial z) = -0.8 \text{ km}^{-1}. \qquad (6.3)$$

Because $\bar{q}$ goes from about 5 g kg^{-1} near the bottom of the transition layer to about 2.5 g kg^{-1} at the highest radar range gate, (6.2) and (6.3) can be used to find α_r^2, which ranges from 1.4 at the bottom to 1.9 at the top. Thus, the $\alpha_r^2 = 1$ assumption may overestimate C_q^2 by as much as a factor of 2 in the upper part of the radar domain.

Note that one could use a mean profile of α_r^2 computed from the average θ–q profiles recorded by the ensemble of radiosondes taken during the experiment. Remember that the turbulence itself produces small-scale gradients that must be removed by averaging before applying (6.2). Unfortunately, the collection of soundings used is not a proper ensemble of independent realizations of equivalent conditions, but includes a variety of different conditions. Also, we have averaged over gravity-wave–induced variability, which is responsible for much of the clear-air turbulence that has been observed (Fairall 1990). An alternate approach

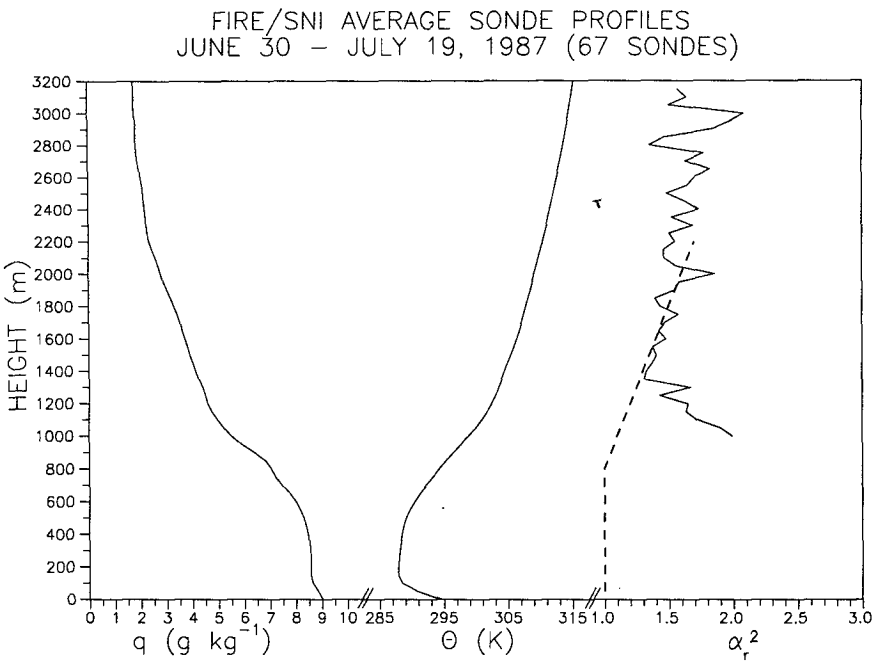

FIG. 3. Average profiles of q (g kg^{-1}) (left) and θ (K) (center) determined from 67 rawinsondes launched 30 June–19 July 1987. Median profile of α_r^2 (right) and smoothed profile of α_r^2 (dashed line) used in calculating C_q^2 from (3.9).

is to compute α_r^2 from each individual sounding after smoothing in the vertical, in order to remove the small-scale gradients associated with the turbulence while leaving the larger-scale variability associated with gravity waves. An estimate of the appropriate vertical resolution for this smoothing can be obtained from the buoyancy subrange scale (Gregg 1987), $L_b \propto (\epsilon/N_b^3)^{0.5}$, which is on the order of 30 m for the free troposphere (Fairall 1990). Since the radiosonde data used has roughly a 50-m height resolution, the raw data will be considered as appropriately smoothed by the sampling and the response time of the sensors. The resulting median profile of α_r^2 is shown in Fig. 3. Figure 4 shows probability and cumulative probability distributions of α_r^2 computed at 1.0, 1.5, and 2.0 km. For a lognormally distributed variable, 68% of the observations are expected to be within one standard deviation of the median, or about a factor of 2.0 for α_r^2 for this data. The actual α_r^2 variability will be reduced for the radar because of vertical smoothing by the 150-m pulse length.

To produce more accurate C_q^2 values, the median profile of the α_r^2 profile was used to compute C_q^2 from the measured radar scattering cross section. A smoothed version of the measured median α_r^2 profile, indicated by the dashed line in Fig. 3, was used down to a height of 800 m; a constant value of 1.0 was assumed below that. Note that this correction must be considered as specific for this particular experiment. For example, an average α_r^2 profile (not shown) computed from 128 high-resolution radiosondes taken in the fall of 1983 at State College, Pennsylvania, indicated that $\alpha_r^2 < 1.3$ up to an altitude of 3.5 km. In contrast to the dry troposphere associated with the persistent subsidence of the summer California coastal regime, the strong convection in Pennsylvania leads to a moister lower troposphere.

b. *Cloud-droplet contributions to* η

The possible cloud-droplet contamination of the refractive-index turbulence (C_n^2) interpretation of the radar return can be estimated by using the standard Rayleigh scattering approximation for spherical particles (Battan 1973),

$$\eta = \pi^5 \lambda^{-4} |K|^2 Z_p, \tag{6.4}$$

where $|K|^2 = 0.93$ is the refractive-index factor for liquid water, λ is the radar wavelength, and Z_p is the so-called radar reflectivity factor,

$$Z_p = \int_0^\infty (2r)^6 n(r) dr, \tag{6.5}$$

where r is the droplet radius and $n(r)$ the droplet-size spectral density. In the radar community, it is common to represent the reflectivity factor as dBZ:

$$\mathrm{dBZ} = 10 \log(Z_p) + 180, \tag{6.6}$$

where the factor 180 results because Z_p is expressed in

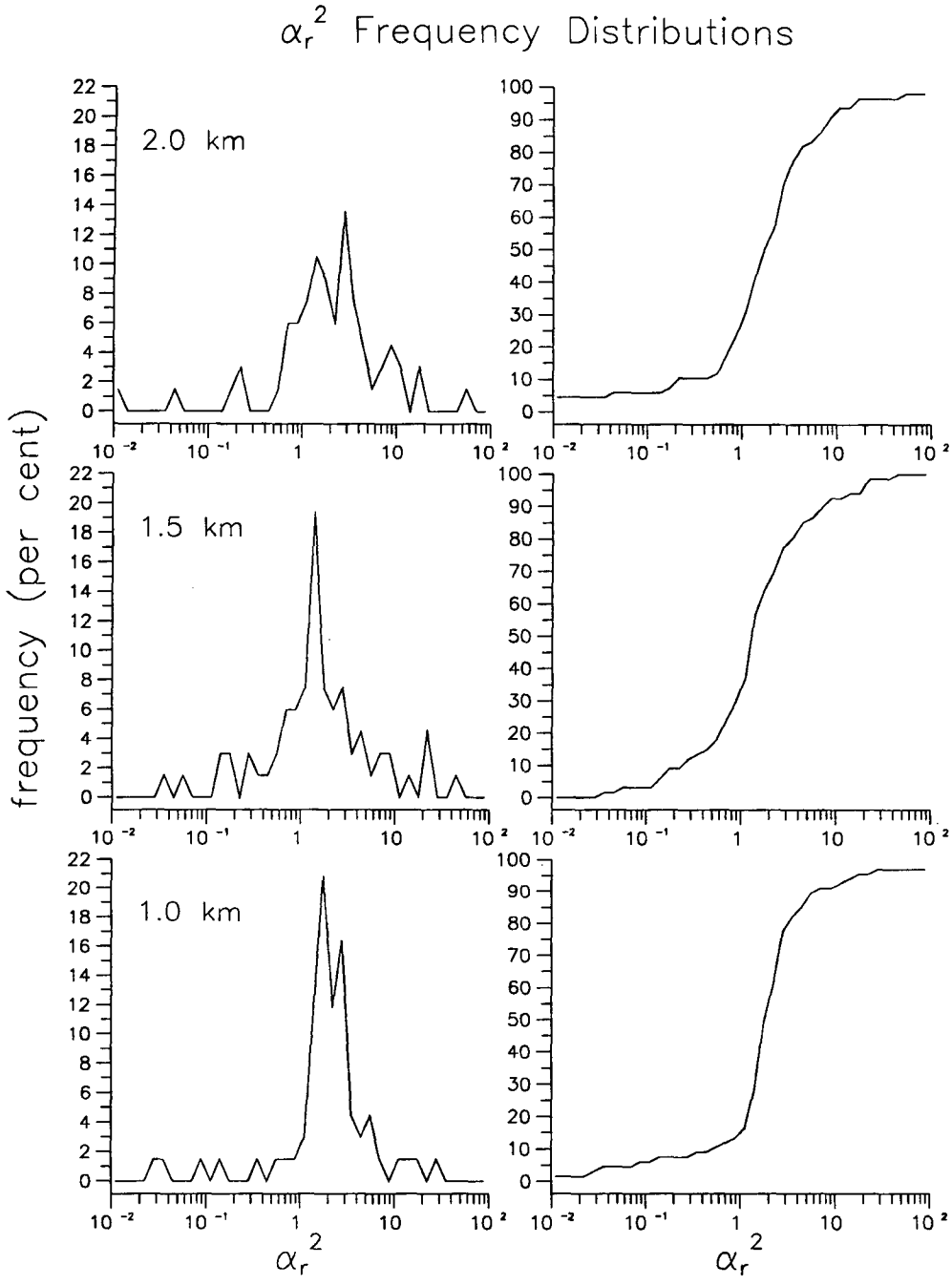

FIG. 4. Probability and cumulative probability distribution functions for α_r^2 determined from 67 rawinsondes launched during the FIRE IFO.

units of cubic meters (m^3) in (6.5), while the dBZ notation assumes conventional units ($mm^6\ m^{-3}$).

Computation of η using (6.4) and (6.5) is straightforward, but it requires a specification of the cloud-droplet spectrum. Here a distinction must be made between actual cloud droplets, which are formed by condensation on hygroscopic aerosols (cloud condensation nuclei or CCN), and drizzle droplets, which are formed primarily by coalescence of cloud droplets (Twomey 1977; Nicholls 1987). Assume that the overall droplet distribution in the cloud can be represented by the sum of two Gaussian distributions: one for the smaller nonprecipitating cloud droplets and one for the larger drizzle droplets. This designation is somewhat arbitrary but is supported by observations (Nicholls 1984; Gossard et al. 1990) and simplifies our

computations. The boundary-layer stratocumulus clouds that are typical for the California coastal regime are relatively easy to work with in this regard because they have been extensively studied and their microphysical properties are fairly well represented by equilibrium adiabatic thermodynamics (Albrecht et al. 1990).

To evaluate the scattering by cloud droplets only, a mixed-layer model developed specifically for stratocumulus was used (Davidson et al. 1984). This model has been shown to be a good representation for the optical properties of the SNI/FIRE clouds (Fairall et al. 1990b). The model uses a lognormal droplet spectrum with an adiabatic (linear) cloud liquid-water content q_l profile. The total number of cloud droplets per unit volume N and the width of the log-Gaussian σ_x are held constant with height in the cloud. The spectrum takes the form

$$n(x) = N[\sigma_x(2\pi)^{1/2}]^{-1} \times \exp[-(x - x_m)^2/2\sigma_x^2], \quad (6.7)$$

where $x = \ln(r)$ and $x_m = \ln(r_m)$ define the number-density mode radius of the distribution. The kth moment of this distribution is

$$\langle r^k \rangle = N^{-1} \int r^k n(x)dx = r_m{}^k \exp(k^2\sigma_x^2/2). \quad (6.8)$$

The liquid-water content at some height in the cloud and the reflectivity factor are computed from the third and sixth moments

$$q_l = (4\pi/3)\rho_w N\langle r^3 \rangle = (4\pi/3)\rho_w N r_m{}^3 \exp(9\sigma_x^2/2) \quad (6.9a)$$

$$Z_p = 2^6 N\langle r^6 \rangle = 2^6 N r_m{}^6 \exp(18\sigma_x^2), \quad (6.9b)$$

where ρ_w is the density of liquid water. Because the droplet concentration is roughly constant while the liquid water increases linearly with height within the stratocumulus cloud, the mode radius increases with height (Fairall et al. 1990b). Equation (6.9a) can be used to eliminate the radius dependence and to obtain an expression for η in terms of the liquid-water content

$$\eta = (9/2)(2\pi)^3\lambda^{-4}|K|^2N^{-1}(q_l/\rho_w)^2 \exp(9\sigma_x^2). \quad (6.10)$$

Typical marine stratocumulus have maximum liquid-water contents between 0.1 and 1.0 g m^{-3} and N between 50 and 200 cm^{-3}. The maximum in liquid water usually occurs near cloud top. Using $\sigma_x = 0.35$, Fairall et al. (1990b) found a best fit to the SNI/FIRE cloud optical thickness and liquid-water relationship for $N = 175$ cm^{-3}. The SNI droplet concentrations are thought to be on the high side due to increases in the CCN associated with the proximity of SNI to the coast. The largest value for q_l observed during FIRE was on the order of 1.0 g m^{-3}. Thus, the maximum value likely to be encountered at SNI during FIRE is $\eta \approx 2.5 \times 10^{-16}$ m^{-1}, which is the turbulence scattering equivalent of $C_q^2 \approx 1 \times 10^{-5}$ g^2 kg^{-2} m$^{-2/3}$. Values of C_q^2 rarely fall below 5×10^{-4} in the cloud-free MABL. Clouds are expected to lead to increased values of C_q^2 near the inversion due to the enhanced mixing associated with cloud-top entrainment. The analysis of the radar data in section 8 shows that during cloudy conditions, the inferred values of C_q^2 in and below the inversion region are at least an order of magnitude larger than the anticipated maximum associated with cloud-droplet scattering considered by itself. In reference to the accuracy of this cloud model, we conclude that our results are not contaminated by cloud-droplet scattering.

Boundary-layer stratocumulus clouds in this region are also known to produce drizzle observable on the ground approximately 5% of the time the clouds are present (Brost et al. 1982). Since drizzle drops are fairly small, they may only survive a few hundred meters below cloud bottom before evaporating. Thus, we expect that considerably more than 5% of stratocumulus clouds actually contain drizzle. Drizzle was not observed on the ground during the analysis period presented in this paper. Furthermore, nearly adiabatic integrated liquid-water contents were measured with a ground-based microwave radiometer during this period (Albrecht et al. 1990). This indicates that only negligible amounts of water were being removed from the cloud by drizzle processes and implies that only a small fraction of the cloud liquid water was partitioned into a drizzle component. For the purposes of this calculation, a drizzle concentration $q_l = 0.1$ g m^{-3} is assumed. However, since drizzle droplets are much larger than cloud droplets (on the order of 50 μm radius versus 5–10 μm), they are much more effective radar scatterers.

The drizzle scattering can be estimated with the same basic approach used for the cloud droplets, except (6.9a) will be used to eliminate N rather than r_m

$$\eta = 3(2\pi/\lambda)^4|K|^2(q_l/\sigma_w)r_m{}^3 \exp(27\sigma_x^2/2). \quad (6.11)$$

Direct measurements of drizzle spectra in marine stratocumulus are considerably rarer than measurements of cloud-droplet spectra. The modeling and observational study by Nicholls (1987) is used. His results suggest that σ_x for drizzle is not significantly different than for cloud droplets and that the mode radius for drizzle flux (roughly the fourth moment of the distribution) is on the order of 60 μm for a cloud with a peak liquid-water concentration of 0.8 g m^{-3}. This implies a number density mode radius $r_m \approx 50$ μm. A droplet of this size has a fall velocity of about 0.5 m s^{-1}, which, combined with the assumed $q_l = 0.1$ g m^{-3}, implies a latent heat flux loss by drizzle from the cloud on the order of 125 W m^{-2}. Such a drizzle rate is probably too great for the extremely persistent stratocumulus encountered at SNI during most of the FIRE

period. Hence, our estimates of drizzle scattering, despite their crudeness, should provide a reasonable upper limit on the effect. With $q_l = 0.1$ g m^{-3}, $r_m = 50$ μm, and $\sigma_x = 0.35$, we obtain $\eta = 4 \times 10^{-16}$ m^{-1}. As in the case of cloud particles, this is less than the anticipated turbulence scattering. However, from (6.11) it can be seen that substantially greater values of q_l or modestly greater values of r_m will be sufficient for drizzle to be detectable over the MABL turbulence background for this wavelength radar.

7. Mean humidity data

Figure 5 is a contour plot of q (g kg^{-1}) for the 120-h period covering 1200 UTC 10 July–1200 UTC 15 July. This analysis used 26 of the 28 rawinsondes launched during this period. The actual launch times are indicated by asterisks at the bottom of Fig. 5. Contour plots were obtained using SURFER™ software. To preserve the data integrity in the contour plot, the raw data were splined by linear interpolation to a 50-m vertical and 1-h temporal resolution before plotting. Detail in the humidity structure during the second half of the period is compromised somewhat by the decreased rawinsonde launch frequency.

8. Radar data analysis

a. Radar data

Figure 6 is a contour plot of $\log_{10}(C_q^2)$ g^2 kg^{-2} m$^{-2/3}$ corresponding to the same time period shown in Fig. 5. Because of a blown fuse in the radar transmitter, data after 114 h were discarded. Hourly medians of radar SNR were produced from the 2-min resolution raw data. Values of C_q^2 were then obtained from (3.9). For consistency, these data were splined to 50-m vertical resolution by linear interpolation. Some additional smoothing (using a 3-point × 3-point smoothing matrix) was performed to make visualization easier. Data below 600 m are not shown because of the radar's loss of sensitivity near its minimum detectable range.

One of the notable features evident in both Figs. 5 and 6 is the position of the marine inversion. The inversion is indicated by the region with enhanced vertical humidity gradients in Fig. 5 and by the height of locally maximized C_q^2 in Fig. 6. Referring to Fig. 5, the base of the inversion was at about 950 m at the beginning of the period, lowered to about 500 m on 13–14 July, and returned to 750 m by the end of the period. Another interesting feature is the drying that can be seen well above the inversion until about 90 h

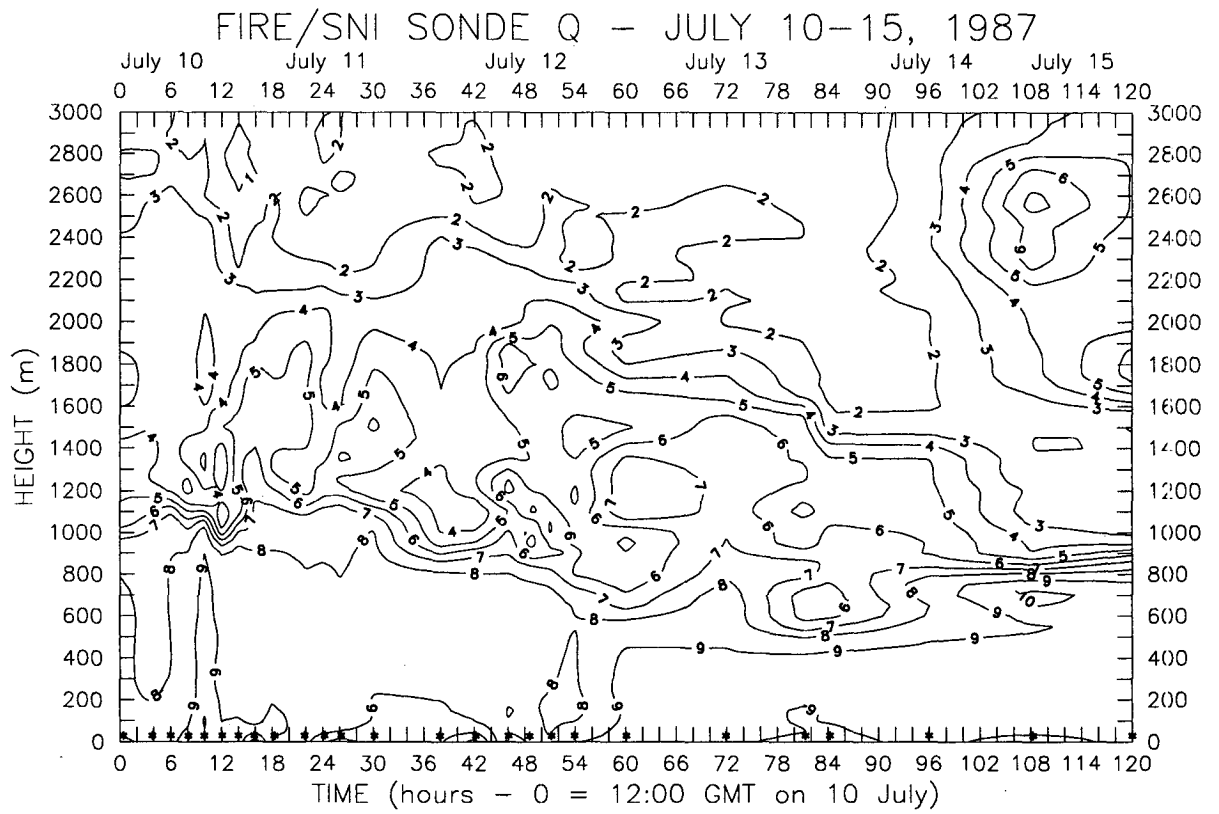

FIG. 5. Contours of specific humidity (g kg^{-1}) calculated from SNI rawinsonde data. Actual rawinsonde launch times (asterisks) are shown along the bottom of the figure.

into the period. Thereafter, rapid moistening occurred. The general downward sloping of the upper-altitude contours indicates steady subsidence aloft.

b. *Radar–sonde correlation analyses*

The rawinsonde and radar data fields used to produce the contour plots shown in Figs. 5 and 6 were used in the following correlation studies. The first study verifies statistically the theoretically expected correlation between C_q^2 and $(\partial q/\partial z)^2$ [see (5.1)], and the second shows a somewhat curious correlation between C_q^2 and q. For these studies, a correlation coefficient ≥ 0.2 is significant at the 95% confidence level.

The correlation as a function of height between $\log(C_q^2)$ and $\log[(\partial q/\partial z)^2]$, shown in Fig. 7, was computed in the following manner. Let $X(z_r)$ denote the time series of $\log(C_q^2)$ at height z_r and $Y(z_s)$ denote $\log[(\partial q/\partial z)]^2$ at height z_s, then the correlation coefficient of the two time series as a function of height, $r(z_r, z_s)$, can be written as

$$r(z_r, z_s) = \{[\overline{X(z_r)Y(z_s)}] - [\overline{X(z_r)}][\overline{Y(z_s)}]\}(\sigma_X\sigma_Y)^{-1}, \quad (8.1)$$

where σ_X^2 and σ_Y^2 are the variances for the two time series, and the overbar represents a time average. Figure 7 shows contours of $r(z_r, z_s) \geq 0.2$. The time series used in this correlation analysis are the same interpolated time series that were used to generate the plots shown in Figs. 5 and 6, except that the matrix smoothing applied for Fig. 6 was omitted.

As expected theoretically, the line of maximum correlation is represented roughly by an imaginary diagonal drawn from the lower left-hand corner to the upper right-hand corner of the plot. The fact that the correlation is not higher along the diagonal may be attributed to certain sampling characteristics of the analyzed data, including the length of time series examined, the gaps in rawinsonde data, and the differences in temporal and vertical resolution in the raw data. There is perhaps a more physical explanation for the degradation in correlation. Equation (5.1) shows that perfect correlation (correlation coefficient = 1) between time series of C_q^2 and $(\partial q/\partial z)^2$ can occur only if C_u^2 and N_b^2 are nonvarying in time. Above the inversion, variations in N_b^2 are small compared to variations in C_u^2. As mentioned earlier, C_u^2 is a direct measurement of the local turbulence and is related to the rate of dissipation of turbulent kinetic energy ϵ by

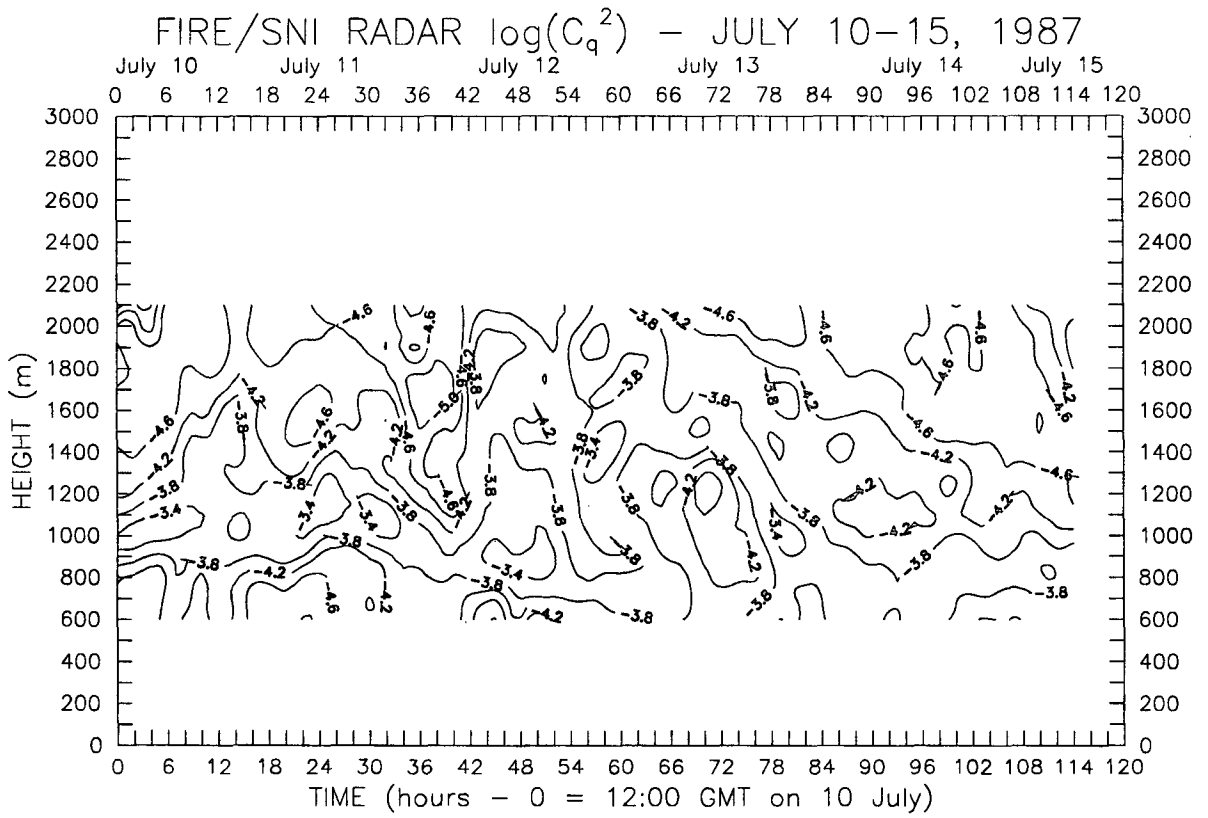

FIG. 6. Contours of $\log(C_q^2)$ ($g^2\ kg^{-2}\ m^{-2/3}$) calculated from SNI radar reflectivity data.

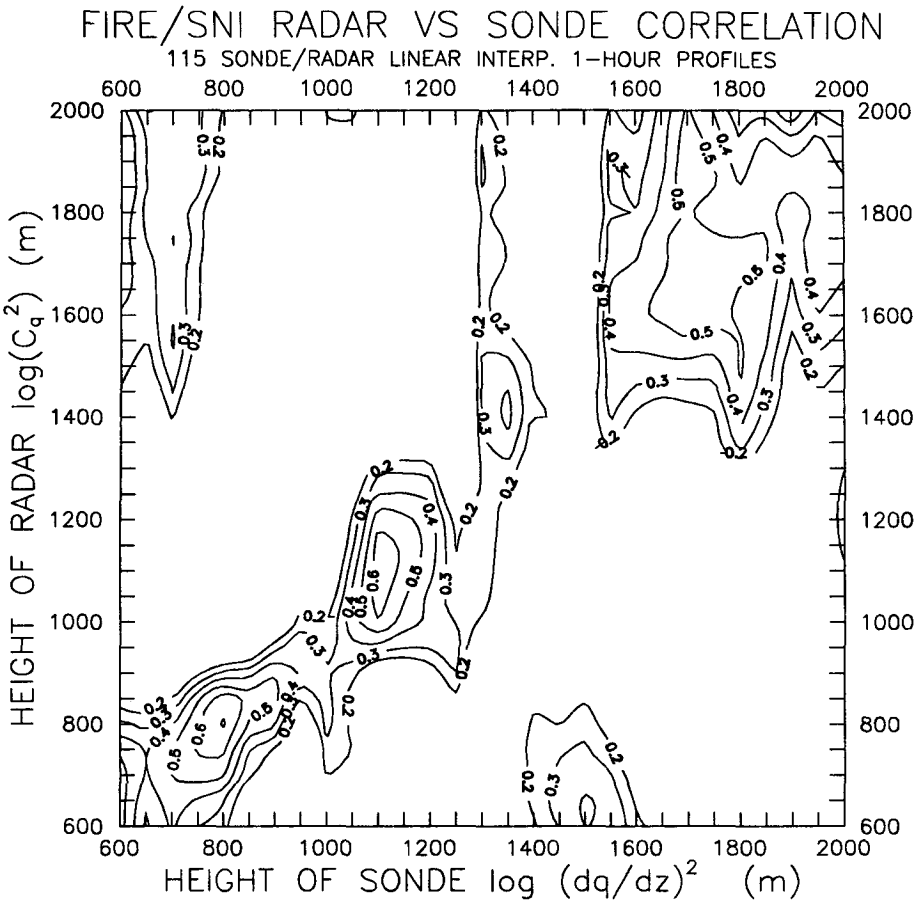

FIG. 7. Correlation as a function of height between radar $\log(C_q^2)$ and $\log(\partial q/\partial z)^2$ determined from rawinsonde data.

$$C_u^2 = 2.0\epsilon^{2/3}. \quad (8.2)$$

A time series of C_u^2 was generated from (5.1) using the radar-derived values of C_q^2 and rawinsonde profiles of $(\partial q/\partial z)^2$ and N_b^2. Contours of C_u^2 for the period analyzed are shown in Fig. 8. An analysis of the standard deviation of C_u^2 as a function of height (not shown) indicated that correlation between C_q^2 and $(\partial q/\partial z)^2$ was at least partially influenced by C_u^2 variability.

The correlation between C_q^2 and $(\partial q/\partial z)^2$ associated with the inversion layer is slightly higher, but it falls off more rapidly with changes in relative height between the radar and the sonde than does the correlation associated with the free troposphere. These features are associated with the more frequent occurrence of coincident "spikes" in radar and sonde data at the fixed altitudes near the inversion. The inversion is marked by strong signals in both C_q^2 and $(\partial q/\partial z)^2$. However, the free troposphere characteristically has weaker gradients and turbulence, which results in lower values of C_q^2. Another factor that may have contributed to the spread and decrease in correlation aloft was the drift of the rawinsondes away from the radar beam.

An additional correlation contour plot, shown in Fig. 9, is produced using (8.1), but with the substitution $Y(z_s) = \log(q)$. Correlation between C_q^2 and q is not unexpected because both variables decrease with height in the mean. Since correlation between C_q^2 and $(\partial q/\partial z)^2$ has already been seen, if correlation existed between q and $(\partial q/\partial z)^2$, we would expect to see correlation between C_q^2 and q. Correlation analysis between q and $(\partial q/\partial z)^2$ (not shown) yielded values of $r \approx 0.3$ above 1300 m. However, an unexpected result of the C_q^2 versus q analysis was that the highest correlation occurred when there was an offset of about 200 m between the radar and sonde in both the inversion and the free troposphere. The significance of this is unclear, but the reason for lobes of high correlation appearing off the diagonal may be a combination of the limited sampling size and the overall stratified nature of the humidity field.

One possible explanation for the height offset in the q correlation is that the inversion C_q^2 peaks correlate with the highest values of humidity. In a marine environment, the highest values of humidity are located somewhere below the inversion in the well-mixed

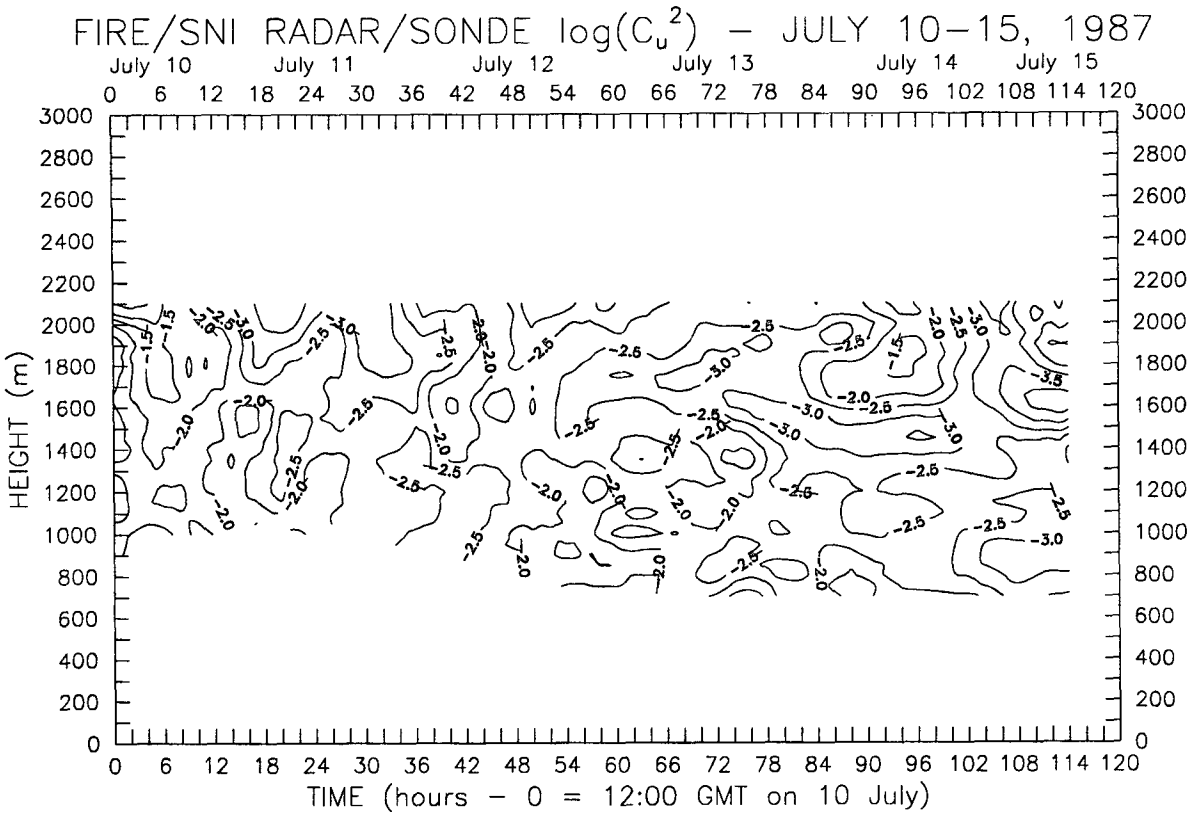

FIG. 8. Contours of $\log(C_u^2)$ ($m^2\ s^{-2}\ m^{-2/3}$) calculated from SNI radar reflectivity and rawinsonde data.

boundary layer. Above the inversion, where the humidity field exhibits more variability, the size of the dataset becomes increasingly important. A small dataset used in this type of analysis will allow short-lived episodes of high correlation between the two time series at different heights to dominate the correlation pattern. For example, the peaks in C_q^2 above 1700 m shown in Fig. 6 from 42 to 66 h correlate well with the humidity gradient in that region. However, at the same time, the peaks in the humidity field are located at much lower heights, between 1200 and 1300 m, as shown in Fig. 5. This coincidental correlation between the elevated C_q^2 peaks and the lower q peaks during this period leads to the smaller of the two $r = 0.6$ correlation lobes found in Fig. 9.

c. *Interpretation of a clearing event*

Although the highest correlation between C_q^2 and $(\partial q/\partial z)^2$ occurs in the inversion layer, it is not the presence of a substantial humidity gradient alone that is responsible for the observed enhancements in C_q^2. A closer analysis of a short-lived clearing event near 40 h helps clarify this point.

Figures 10 and 11 are expanded sections of the contour plots shown in Figs. 5 and 6, respectively. In Fig. 11, between 36 and 41 h, notice the decreased values of $\log(C_q^2)$ in the inversion, evidenced by the absence of contours labeled ≥ -3.6. At the same time, Fig. 10 shows a tight packing of q contours in the inversion. In light of (5.1) and (5.2), this presents somewhat of a puzzle. Why does C_q^2 (or w_e) decrease in a region of locally enhanced $(\partial q/\partial z)^2$ (or Δq)? To uncover the answer, one needs to look at some of the other data collected at SNI during FIRE.

In addition to the CLASS system, CSU operated a lidar ceilometer (Schubert et al. 1987b). Figure 12 shows a record of cloud base derived from the lidar reflectivity. Clear sky is depicted by a point at 960 m. The temporal and vertical resolution in Fig. 12 is 30 s and 15 m, respectively. Notice the descent of the cloud base from 36 to 40 h and a brief clear period between 39 and 41 h.

To further define the transition of this cloud layer, Fig. 13 shows a time series of the downwelling longwave irradiance monitored with a standard Eppley pyrgeometer. The reduction in irradiance between 34 and 42 h can be attributed to a reduction in emissivity associated with thinning of the cloud layer. As the cloud

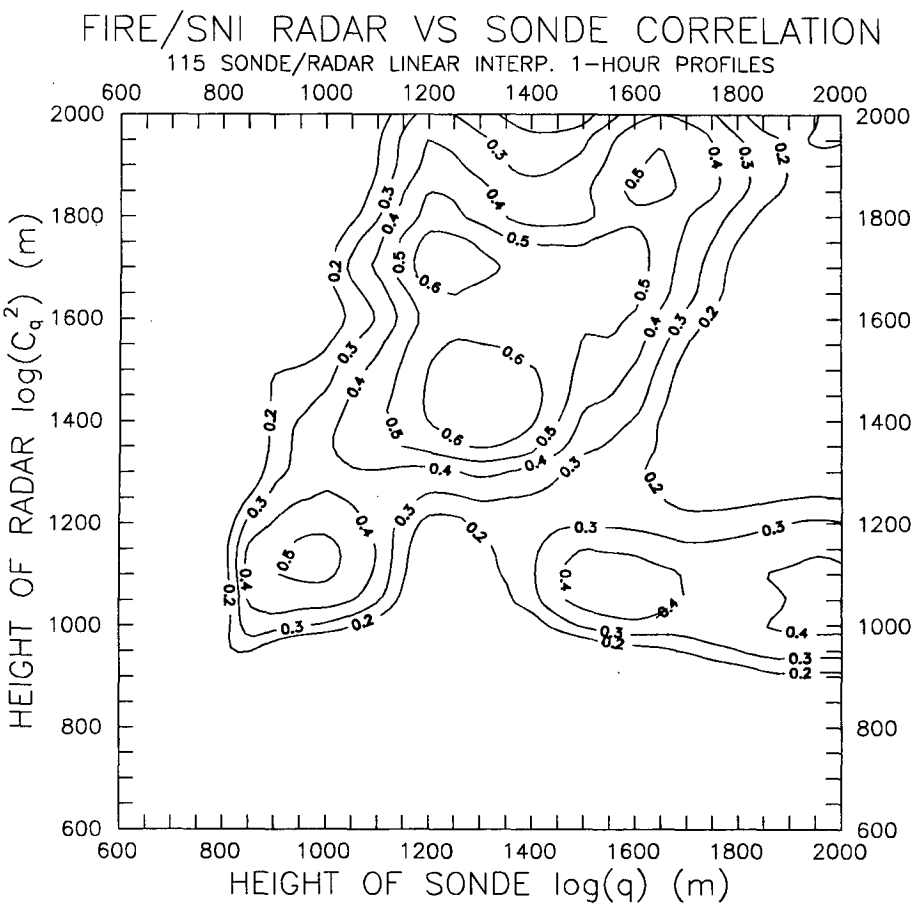

FIG. 9. Correlation as a function of height between radar $\log(C_q^2)$ and $\log(q)$ determined from rawinsonde data.

layer dissipated, the longwave, cooling-induced convection that drives cloud-top entrainment diminished.

Another potential source of energy for driving cloud-top entrainment is the vertical wind shear that is often present near the inversion interface. Wind-speed contours from the merged sodar–wind profiler dataset (Syrett 1988) are shown in Fig. 14. The period from 35 to 41 h had both light winds and negligible wind shear.

Since entrainment is the primary mechanism by which gradients in the inversion are turbulently mixed, a reduction in entrainment should result in lower values of C_q^2 even if the inversion humidity gradient remains strong. In this example, the radar C_q^2 data clearly indicate a substantial reduction in the entrainment rate associated with a diminishing cloud layer.

d. Entrainment rates

The combined radar–rawinsonde datasets were used to calculate w_e from (5.2) for cloudy and clear conditions. Since the primary objective of the FIRE IFO was to study the dynamic structure of marine stratocumulus clouds, only a few rawinsondes were launched throughout the experiment during clear sky conditions. For the 5-day period analyzed here, cloudy conditions prevailed except for the brief clearing near 40 h and, later, a more extended clearing lasted for about 11 h centered on 60 h. The rawinsonde launched near 60 h provided the only available in situ mean profile data recorded during clear conditions.

Values of w_e for the entire analysis period are plotted in Fig. 15. For the clear cases, $\epsilon = 4.0 \times 10^{-4}$ m^2 s^{-3} was assumed. This value was based on aircraft (hot-wire anemometer) data collected earlier near Monterey, California (Fairall 1984). For cloudy conditions, a value of $\epsilon = 1.0 \times 10^{-3}$ m^2 s^{-3} was estimated from model results of stratocumulus-topped boundary layers (Nicholls 1984; Duynkerke and Driedonks 1987; Moeng 1987). Values of C_q^2 at the inversion were determined from the peaks in the hourly averaged vertical profiles of radar reflectivity. All other varibles in (5.2) were determined from the rawinsonde profiles. In Fig. 15, the solid line represents values of w_e calculated from

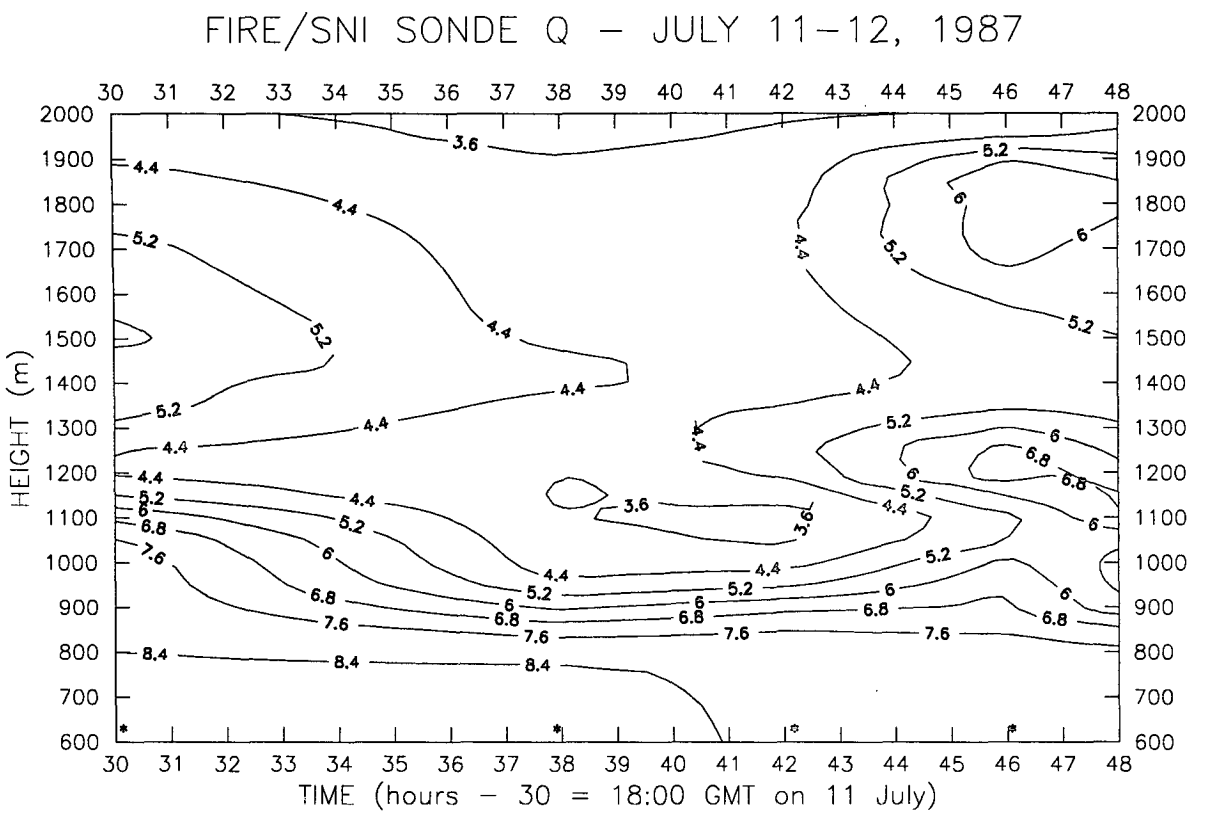

FIG. 10. Enlarged section of Fig. 5 contours of specific humidity (g kg^{-1}) calculated from SNI rawinsonde data. Actual rawinsonde launch times (asterisks) are shown along the bottom of the figure.

radar and rawinsonde data linearly interpolated to 1-h intervals. The period from 77 to 88 h is omitted from the time series because the inversion fell below the radar's minimum usable range.

There is good qualitative agreement between the peaks in w_e shown in Fig. 15 and the changes in humidity structure depicted by the contours shown in Fig. 5. Although questionable in absolute magnitude, the peaks at 16 h and 96 h both correspond to periods when an upward intrusion of moist air resulted in a rapid increase in the height of the inversion. The somewhat lower-valued peaks in w_e occurring just after clearing also correspond to upward intrusions of moist air. Resolution of some of the structure was undoubtedly lost because of decreased sonde launch frequency. The decrease in the inversion height near 73 h corresponds to a sharp drop in w_e. The hypothesized drop in entrainment during the short-lived clearing period analyzed in section 8c is confirmed in Fig. 15 by the local minimum in w_e (0.04 cm s^{-1}) at 40 h.

One way to evaluate the quantitative accuracy of the radar-derived entrainment rates shown in Fig. 15 is to compare the mean entrainment rate for the period with the entrainment rate calculated using a boundary-layer depth equation (Davidson et al. 1984). In the absence of advection, the change with time of the depth of the marine inversion may be expressed as

$$dz_i/dt = w_i = w_e + \bar{w}, \tag{8.3}$$

where $dz_i/dt = w_i$ represents the net rate of change in depth of the marine inversion, and $\bar{w}$ is the average rate of convergence-induced vertical motion above the inversion. This approach is similar to that used by Noonkester (1976).

Referring to Fig. 5, let $\bar{w}$ be represented by the rate of change in height of the 3 g kg^{-1} contour from 0 to 114 h:

$$\bar{w} = (1000 \text{ m} - 2420 \text{ m})(114 \text{ h})^{-1} = -0.35 \text{ cm s}^{-1}. \tag{8.4}$$

This subsidence rate can be divided by the height of the inversion to obtain the horizontal divergence at the top of the mixed layer. Using an average inversion height of 850 m, we calculate a divergence of 4.12 $\times 10^{-6}$ s^{-1}. This value is close to the average value of divergence obtained for the Los Angeles–San Diego basin over a 3-day period (Davidson et al. 1984) in which synoptic conditions were similar to those encountered during FIRE.

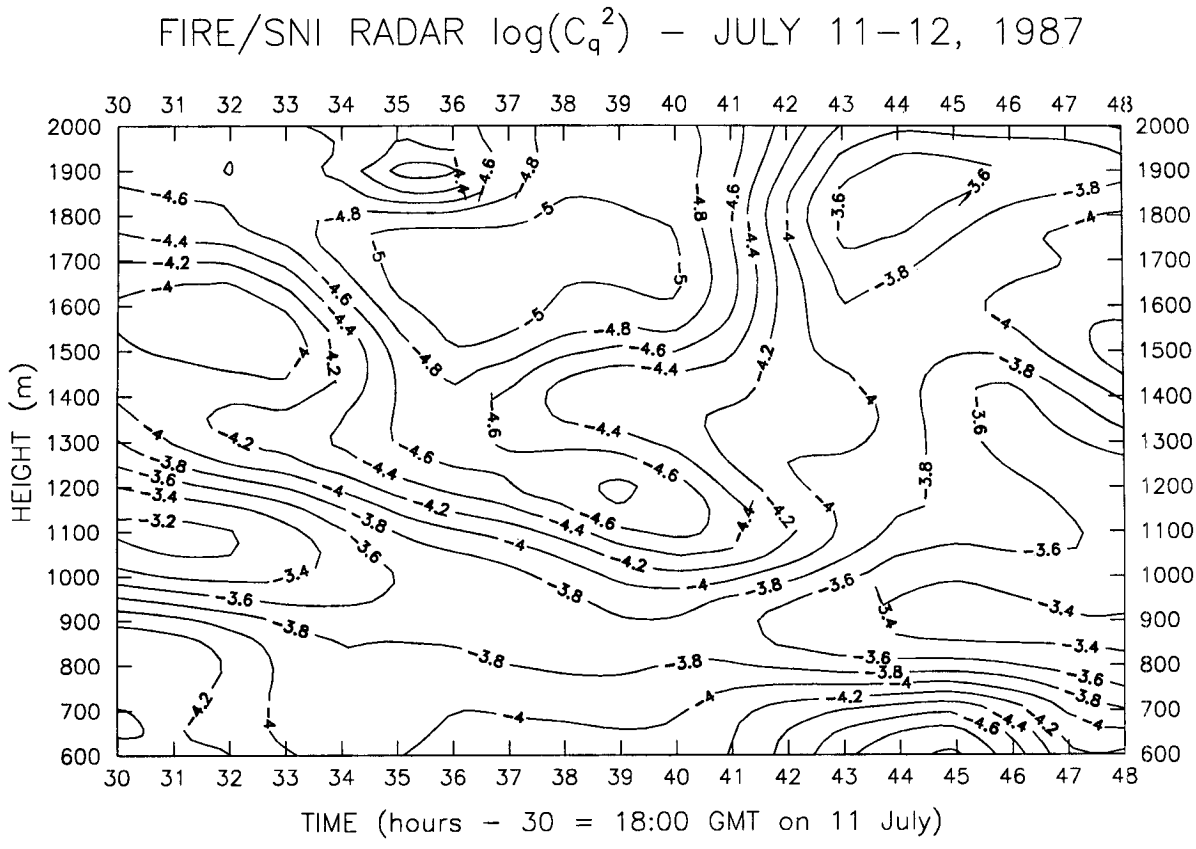

FIG. 11. Enlarged section of Fig. 6 contours of $\log(C_q^2)$ ($g^2\ kg^{-2}\ m^{-2/3}$) calculated from SNI radar reflectivity data.

Next, the rate of change in the inversion height was calculated:

$$w_i = (750\ \text{m} - 950\ \text{m})(114\ \text{h})^{-1} = -0.05\ \text{cm s}^{-1}. \quad (8.5)$$

From (8.3), the difference between w_i and $\bar{w}$ should give a rough estimate of the average MABL growth rate attributable to entrainment at the top of an otherwise nonconvective MABL:

$$w_e = w_i - \bar{w} = -0.05 - (-0.35) = 0.30\ \text{cm s}^{-1}. \quad (8.6)$$

The average entrainment rate determined from the entire time series of hourly interpolated radar–rawinsonde data is

$$w_e = 0.29\ \text{cm s}^{-1}. \quad (8.7)$$

Thus, the characteristic humidity structure present during the analyzed period allows comparison of the mean entrainment rate derived from (5.2) with the average descent of the marine inversion. The above single comparison should not be considered conclusive, especially since this simple model neglects any advective effects. However, the excellent agreement between the two independent calculations provided by evaluation of (8.6) and (8.7) suggests the feasibility of using radar reflectivity data to estimate w_e. Furthermore, since the entrainment velocity derived from (5.2) is proportional to α_u^2, we conclude that our calibration of the radar was reasonably accurate.

9. Summary and conclusions

This paper presents an analysis of the humidity structure at the top of the MABL and in the overlying free troposphere using Doppler radar reflectivity and conventional rawinsonde data collected at SNI during the FIRE IFO. Vertical profiles of radar C_q^2 and rawinsonde $(\partial q/\partial z)^2$ were used in a correlation analysis that statistically verified the theoretically expected correlation expressed in (5.1). Correlation between the two time series was highest in the inversion region where vertical humidity gradients were largest. Perhaps the most important result was that regions of high correlation were shown to consistently fall along a line of zero height lag between the two instruments. This correlation was observed despite roughly a factor of 2

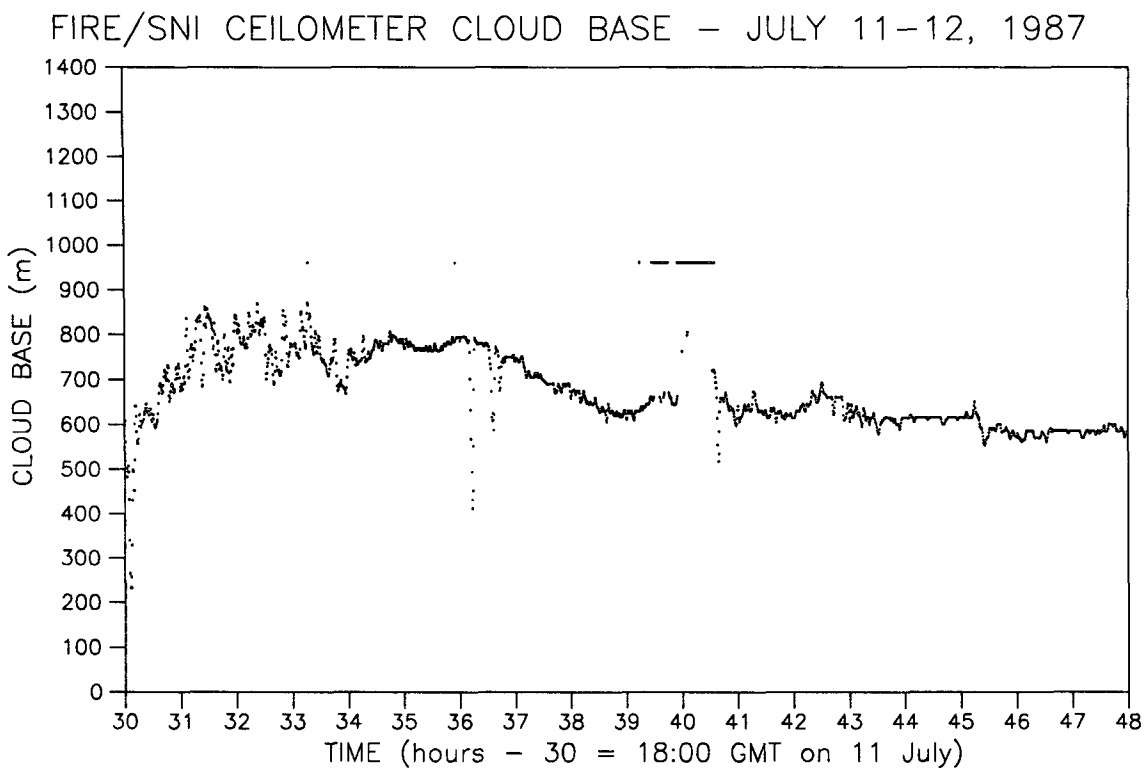

FIG. 12. Time series of cloud-base height (m) measured by the ceilometer located at SNI.

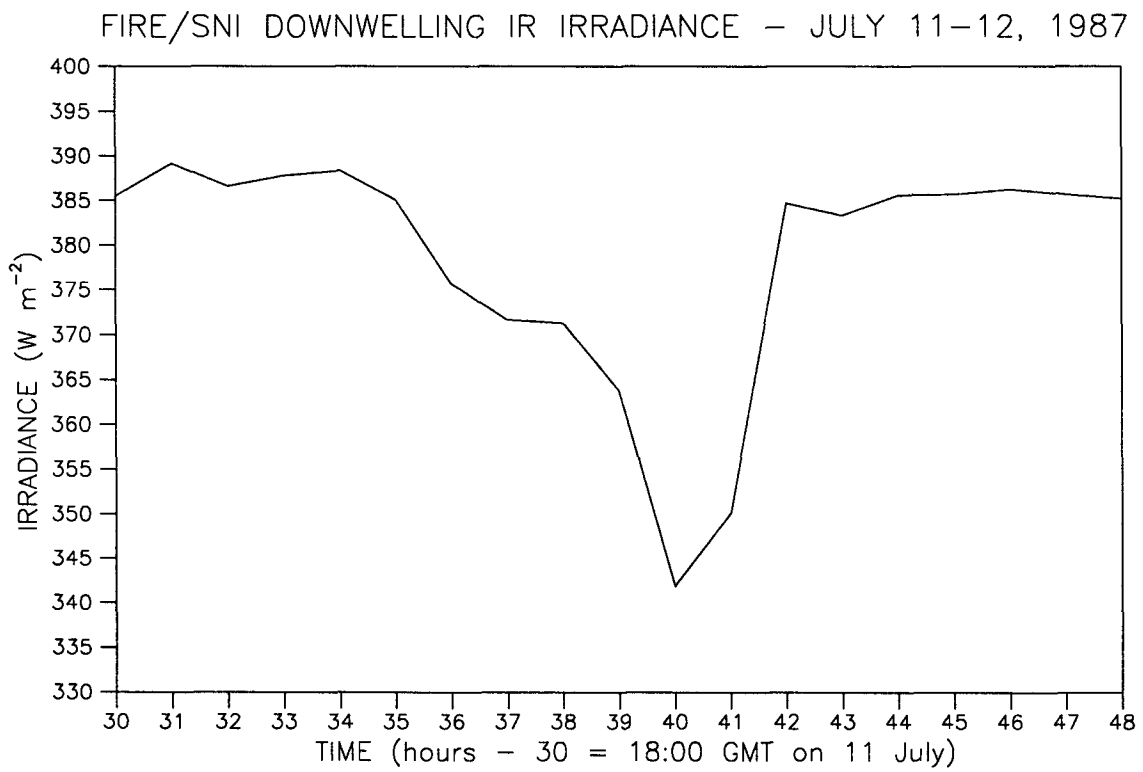

FIG. 13. Time series of downwelling, longwave irradiance (W m^{-2}) measured by a standard Eppley pyrgeometer located at SNI.

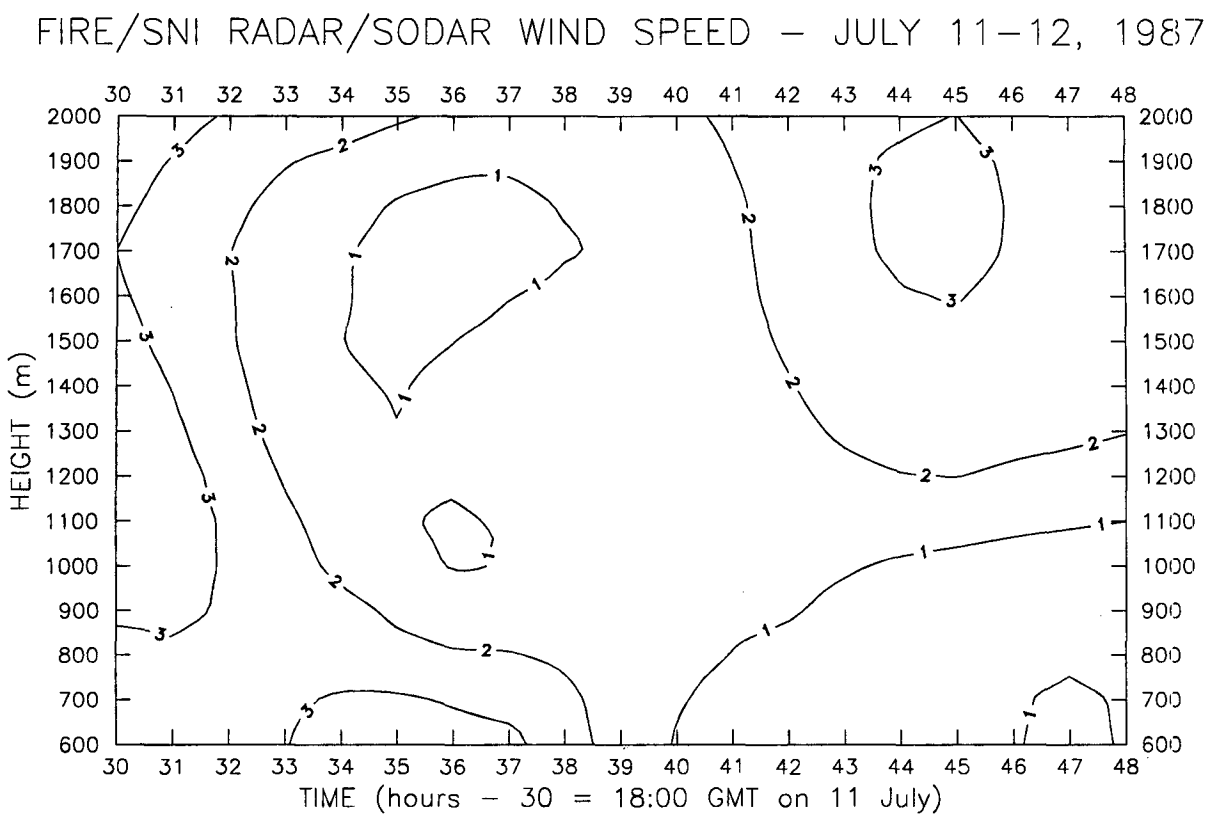

FIG. 14. Contours of merged radar–sodar horizontal wind speed (m s^{-1}).

variations in both C_u^2 and α_r^2: parameters that enter the functional relationship between radar-derived C_q^2 and $(\partial q/\partial z)^2$.

Closer analysis of a short-duration clearing event showed inversion values of C_q^2 decreasing in a region of enhanced $(\partial q/\partial z)^2$. The decrease in C_q^2 was explained by the temporary absence of the cloud-top radiative cooling needed to drive the entrainment process. Entrainment normally enhances the mixing at the inversion interface.

Using rawinsonde-derived values for $\Delta\theta_v$, Δq, and Γ, radar C_q^2 data were used to calculate a time series of w_e. The results of this calculation were shown in Fig. 15. Although highly variable, the time series of radar-derived entrainment rates agree qualitatively with features of the marine inversion structure that are evident in the contoured humidity data. Encouraging results were also obtained from a direct comparison of the mean radar-derived entrainment rate for the 5-day period and the difference between the average subsidence rate deduced from the descent of moisture features above the inversion and the observed boundary-layer growth rate.

These results suggest the potential utility of using clear-air radar backscatter intensity, combined with data from other sources, to infer information about atmospheric humidity structure and important turbulent processes such as entrainment. However, before this potential can be fully realized, several issues must be resolved. First, an accurate calibration of the radar system efficiency is needed. Secondly, the contributions of α_r^2 and C_u^2 to radar C_n^2 must be clearly understood. Evaluation of these factors requires independent coincident measurements to ensure proper representation of the conditions present during operation of the radar. Recent improvements in radar antenna design have reduced the amount of antenna ringing inherent to pulsed systems. The resulting increased radar sensitivity in the lower range gates may partially solve the calibration problem by allowing, for example, comparison of radar reflectivity data to in situ measurements of wind, temperature, and humidity made by instruments fixed on a tower. Operational difficulties during the SNI program, the first maritime operation of a wind profiler, precluded a more detailed and conclusive comparison with in situ turbulence measurments. However, the Atlantic Stratocumulus Transition Experiment (ASTEX) to be conducted in June 1992 should provide an even better opportunity to study the physical processes governing entrainment above a stratocumulus-topped MABL. During ASTEX, a number of profilers, as well as other remote sensing

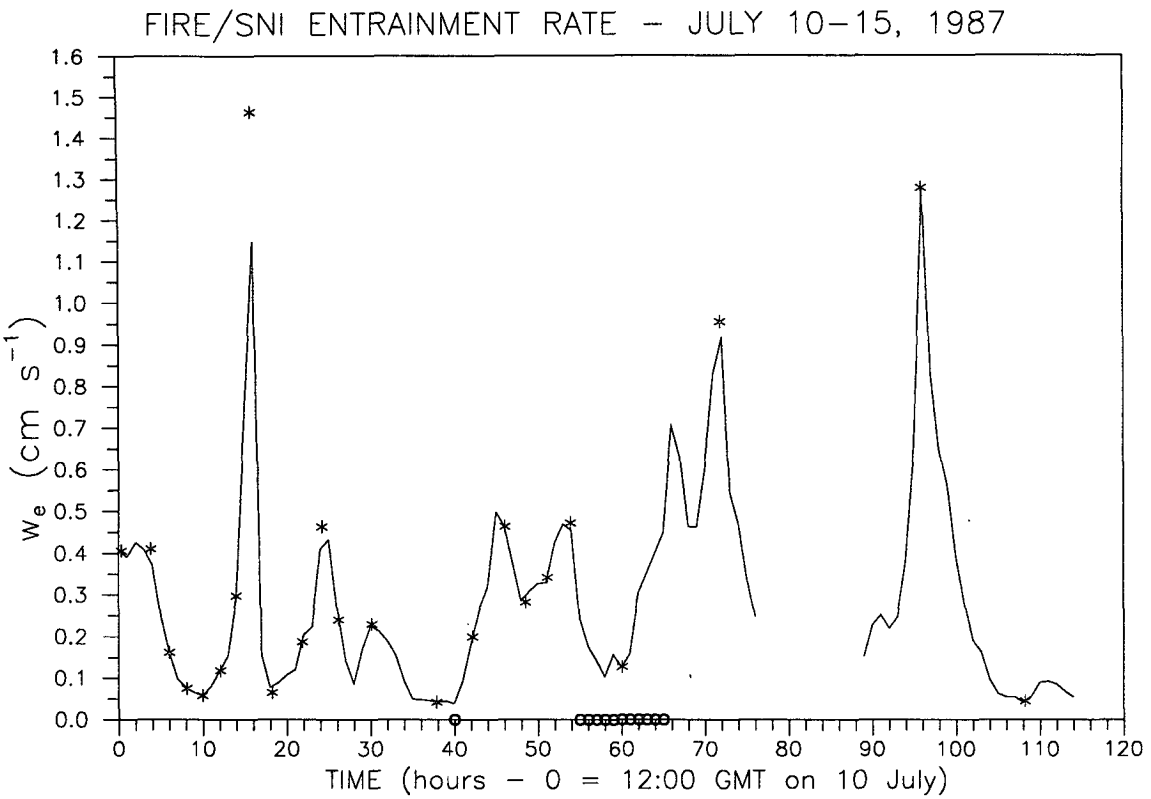

FIG. 15. Time series of w_e (cm s^{-1}) (solid line) obtained from (5.2) using hourly interpolated radar and rawinsonde data. Discrete values of w_e (asterisks) calculated from the uninterpolated rawinsonde profiles. Periods of clear sky conditions (circles) are indicated along the time axis.

systems for monitoring cloud microphysical processes, are to be deployed and remain in continuous operation.

Acknowledgments. With regard to operation of the Penn State Doppler wind profiler and radar data retrieval, the authors gratefully acknowledge the assistance of R. Peters, W. Syrett, R. Thompson, and S. Williams. The critical review and recommendations made by E. Gossard, B. Martner, and R. Strauch are also appreciated. This work was sponsored in part by the Office of Naval Research, ONR Contract N00014-86-K-0688.

REFERENCES

Albrecht, B. A., D. A. Randall and S. Nicholls. 1988: Observations of marine stratocumulus clouds during FIRE. *Bull. Amer. Meteor. Soc.*, **69**, 618–626.

——, C. W. Fairall, D. W. Thomson, A. B. White and J. B. Snider, 1990: Surface-based remote sensing of the observed and the adiabatic liquid water content of stratocumulus clouds. *Geophys. Res. Lett.*, **17**, 89–92.

Battan, L. J., 1973: *Radar Observations of the Atmosphere.* University of Chicago Press, 324 pp.

Beecher, E. A., 1988: Analysis of temperature and velocity microturbulence parameters from aircraft data and relationship to atmospheric refractive index structure. M.S. thesis, The Pennsylvania State University, 165 pp.

Brost, R. A., J. C. Wyngaard and D. H. Lenschow, 1982: Marine stratocumulus layers. Part II: Turbulence budgets. *J. Atmos. Sci.*, **39**, 818–836.

Burk, S. D., 1980: Refractive index structure parameters: Time-dependent calculations using a numerical boundary-layer model. *J. Appl. Meteor.*, **19**, 562–576.

——, 1981: Temperature and humidity effects on refractive index fluctuations in upper regions of the convective boundary layer. *J. Appl. Meteor.*, **20**, 717–721.

Davidson, K. L., C. W. Fairall, P. Jones Boyle and G. E. Schacher, 1984: Verification of an atmospheric mixed-layer model for a coastal region. *J. Climate Appl. Meteor.*, **23**, 617–636.

Duynkerke, P. G., and A. G. M. Driedonks, 1987: A model for the turbulent structure of the stratocumulus-topped atmospheric boundary layer. *J. Atmos. Sci.*, **44**, 43–64.

Fairall, C. W., 1982: An analysis of the Wyngaard–LeMone model of refractive index and micrometeorological structure functions at the top of a turbulent mixed layer. Tech. Rep. NPS63-82-006CR, Naval Postgraduate School, Monterey, California, 101 pp. [Available from C. Fairall, R/E/WP7, NOAA, 325 Broadway, Boulder, CO 80303.]

——, 1984: Wind shear enhancement of entrainment and refractive index structure parameter at the top of a turbulent mixed layer. *J. Atmos. Sci.*, **41**, 3472–3484.

——, 1987: A top-down and bottom-up diffusion model of C_T^2 and C_q^2 in the entraining convective boundary layer. *J. Atmos. Sci.*, **44**, 1009–1017.

——, 1990: A model of gravity-wave-induced variability and tur-

bulence in the stratified free atmosphere. NOAA Tech. Memo. ERL WPL-179, 325 Broadway, Boulder, CO, 65 pp.

——, 1991: The humidity and temperature sensitivity of clear-air radars in the convective boundary layer. *J. Appl. Meteor.*, **30,** 1064–1074.

——, and R. Markson, 1984: Aircraft measurements of atmospheric velocity and temperature microturbulence spectra. Department of Meteorology Tech. Rep., The Pennsylvania State University, 45 pp.

——, D. W. Thomson and R. Markson, 1988: An aircraft and radar study of temperature and velocity microturbulence in the stably stratified free troposphere. Preprints, *Eight Symp. on Turbulence and Diffusion,* Boston, Amer. Meteor. Soc., 61–65.

——, J. B. Edson, S. E. Larsen and P. G. Mestayer, 1990a: Inertial-dissipation air–sea flux measurements: A prototype system using real time spectral processing. *J. Atmos. Oceanic Technol.*, **7,** 425–453.

——, J. E. Hare and J. B. Snider, 1990b: An eight-month sample of marine stratocumulus cloud fraction, albedo, and integrated liquid water. *J. Climate,* **3,** 847–864.

Gossard, E. E., and N. Sengupta, 1988: Measuring gradients of meteorological properties in elevated layers with a surface-based Doppler radar. *Radio Sci.,* **23,** 625–639.

——, R. G. Strauch and R. R. Rogers, 1990: Evolution of dropsize distributions in liquid precipitation observed by ground-based Doppler radar. *J. Tech.*, **7,** 815–828.

Gregg, M. C., 1987: Diapycnal mixing in the thermocline: A review. *J. Geophys. Res.*, **92,** 5249–5286.

Hocking, W. K., 1983: On the extraction of atmospheric turbulence parameters from radar backscatter Doppler spectra. I: Theory. *J. Atmos. Terr. Phys.*, **45,** 89–102.

Kloesel, K. A., B. A. Albrecht and D. P. Wylie, 1988: FIRE marine stratocumulus observations—summary of operations and synoptic conditions. FIRE Tech. Rep. No. 1, Department of Meteorology, The Pennsylvania State University, 171 pp.

Kraus, J. D., 1966: *Radio Astronomy.* McGraw-Hill, 486 pp.

Moeng, C. H., 1987: Large-eddy simulation of a stratus-topped boundary layer. Part II: Implications for mixed-layer modeling. *J. Atmos. Sci.*, **44,** 1605–1614.

Nicholls, S., 1984: The dynamics of stratocumulus: Aircraft observations and comparisons with a mixed-layer model. *Quart. J. Roy. Meteor. Soc.*, **110,** 783–820.

——, 1987: A model of drizzle growth in warm, turbulent, stratiform clouds. *Quart. J. Roy. Meteor. Soc.*, **113,** 1141–1170.

Noonkester, V. R., 1976: Evolution of the clear air convective layer revealed by surface-based remote sensors. *J. Appl. Meteor.*, **15,** 594–606.

Ottersten, H., 1969a: Atmospheric structure and radar backscattering in clear air. *Radio Sci.*, **4,** 1179–1193.

——, 1969b: Mean vertical gradient of potential refractive index in turbulent mixing and radar detection of CAT. *Radio Sci.*, **4,** 1247–1249.

Schubert, W. H., P. E. Ciesielski, T. B. McKee, J. D. Kleist, S. K. Cox, C. M. Johnson-Pasqua and W. L. Smith, Jr., 1987a: Analysis of boundary layer sounding data from the FIRE marine stratocumulus project. Colorado State University Atmospheric Science Paper No. 419, Ft. Collins, CO, 101 pp.

——, S. K. Cox, P. E. Ciesielski and C. M. Johnson-Pasqua, 1987b: Operation of a ceilometer during the FIRE marine stratocumulus experiment. Colorado State University Atmospheric Science Paper No. 420, Ft. Collins, CO, 34 pp.

Strauch, R. G., D. A. Merritt, K. P. Moran, K. B. Earnshaw and D. van de Kamp, 1984: The Colorado wind-profiling network. *J. Atmos. Oceanic Technol.*, **1,** 37–49.

Syrett, W. J., 1988: Hourly wind, potential temperature, and Richardson number profiles at San Nicolas Island during project FIRE. FIRE Tech. Rep. No. 2, Department of Meteorology, The Pennsylvania State University, 49 pp.

Twomey, S., 1977: *Atmospheric Aerosols.* Elsevier Publishing, 302 pp.

VanZandt, T. E., J. L. Green, K. S. Gage and W. L. Clark, 1978: Vertical profiles of refractivity turbulence structure constant: Comparison of observations by the Sunset Radar with a new theoretical model. *Radio Sci.*, **13,** 819–929.

Wesely, M. L., 1976: The combined effect of temperature and humidity fluctuations on refractive index. *J. Appl. Meteor.*, **15,** 43–49.

Wyngaard, J. C., and M. A. LeMone, 1980: Behavior of the refractive index structure parameter in the entraining convective boundary layer. *J. Atmos. Sci.*, **35,** 1573–1585.

——, Y. Izumi and S. A. Collins, 1971: Behavior of the refractive index structure parameter near the ground. *J. Opt. Soc. Amer.*, **61,** 1646–1650.